HighTech and Innovation Journal

ISSN: 2723-9535

Available online at www.HighTechJournal.org

HighTech and Innovation Journal

Vol. 6, No. 4, December, 2025

Experimental and Numerical Modeling of a Cross-Flow Turbine Runner Made of HDPE: Experimental and Numerical Approach

Francis M. Kifumbi [1*], Guyh Dituba Ngoma [1], Fouad Erchiqui [1], Theophile M. Tshibangu [1]

[1] *School of Engineering, University of Quebec in Abitibi-Témiscamingue, Rouyn-Noranda, QC J9X 5E4, Canada.*

Received 01 September 2025; Revised 19 November 2025; Accepted 23 November 2025; Published 01 December 2025

Abstract

This study investigates the viability of high-density polyethylene (HDPE) as a sustainable, low-cost alternative to conventional metallic materials for Cross-flow turbine runners in micro-hydropower systems. The primary goal is to design, manufacture, and validate the hydrodynamic and structural performance of an HDPE runner. A three-stage methodology was applied: CAD-based design, thermoforming fabrication, and performance evaluation through computational fluid dynamics (CFD) and finite element analysis (FEA) using ANSYS. Numerical predictions were validated against experimental data obtained from a hydraulic test bench. Mesh refinement and turbulence modeling were included to ensure numerical reliability. Results show that the HDPE runner achieved efficiencies of 80-83% compared to a geometrically identical steel runner under similar operating conditions. Structural analysis confirmed von Mises stresses (8.5 MPa) and deformations (0.12 mm) remained well below HDPE's yield strength (22 MPa), validating its mechanical integrity. Statistical comparison revealed a deviation of less than 4% between numerical and experimental results. This research provides a validated framework for using recyclable HDPE in turbine manufacturing. It demonstrates that HDPE can deliver comparable power output to steel while reducing manufacturing costs and environmental impact, offering a sustainable pathway for rural electrification.

Keywords: Cross-Flow Turbine; HDPE; Experimental Validation; CFD; FEA; Micro-Hydropower; Sustainable Materials; Flow Harshness.

1. Introduction

Amidst the global energy transition, hydropower remains a crucial source of renewable energy. Within this sector, mini-hydropower plants (< 5 MW) provide reliable solutions for rural and off-grid communities [1, 2]. However, high capital costs associated with mechanical components, particularly turbine runners, continue to limit widespread deployment. Among available turbine types, the Cross-flow (Banki) turbine is widely recognized for its simplicity, robustness, and efficiency under low-head conditions, making it a preferred choice for micro-hydropower applications [3].

Traditionally, runners are manufactured from steel or aluminum, which, despite their mechanical robustness, present significant drawbacks: energy-intensive production, susceptibility to corrosion, and a considerable ecological footprint. Recent studies have investigated ways to improve Cross-flow turbine performance through blade geometry optimization [4] and runner blade count [5], as well as advanced control strategies for turbine arrays [6]. Parallel research has explored

---

* Corresponding author: francis.kifumbi@uqat.ca

http://dx.doi.org/10.28991/HIJ-2025-06-04-01

the use of thermoplastic composites in hydrokinetic and wind turbines, highlighting their mechanical potential under dynamic loading [7]. Furthermore, recycled polymers have been proposed as sustainable alternatives for runner manufacturing in micro-hydropower systems [8].

Despite these advances, HDPE has not yet been systematically evaluated as a runner material for Cross-flow turbines, representing a clear gap in the literature. HDPE offers superior impact resistance, abrasion resistance, and stress tolerance compared to polypropylene (PP) and polyethylene terephthalate (PET), while maintaining low cost, high recyclability, and excellent chemical resistance [9]. These attributes make HDPE particularly promising for turbine blade manufacturing in environments where corrosion and cost are critical concerns [10].

The objective of this work is therefore to design, model, manufacture, and experimentally validate a Cross-flow turbine runner fabricated from HDPE. Using a dual approach—numerical simulations (CFD and FEA) and prototype testing on a hydraulic bench-this study aims to assess whether HDPE can achieve performance comparable to metallic runners while offering significant economic and environmental benefits. By addressing this gap, the research contributes to the development of cost-effective and sustainable solutions for electrification in remote regions.

Recently, the adoption of thermoplastic polymer materials has emerged as a promising alternative. Specifically, high-density polyethylene (HDPE) exhibits excellent potential for turbine blade manufacturing. This material offers several key advantages, including lightweight properties, chemical resistance, low manufacturing cost, and high recyclability [11].

The objective of this study is to design, model, and optimize performance of a Cross-flow turbine runner using HDPE materiel. To achieve this, experimental and numerical approaches are used. First, finite element analysis (FEA) is used to predict structural and hydrodynamic performance of HDPE turbine blades. Secondly, a turbine runner made with HDPE is used and experimentations are conducted on the hydraulic test bench. The aim is to validate results.

This research is grounded in a sustainability-driven innovation framework, with the objective of developing cost-effective and environmentally sustainable hydropower solutions. The optimization of design and manufacturing parameters for High-Density Polyethylene (HDPE) turbines holds significant potential to advance electrification efforts in remote regions while simultaneously minimizing ecological impacts.

The research methodology follows a three-stage approach:

- Design: Numerical modeling of the Cross-flow turbine runner using HDPE materiel;
- Manufacturing: making of Cross-flow runner using HDPE materiel;
- Validation: Comparison of numerical models with experimental prototype results.

2. Classification of Micro-Hydropower Plants

Large-scale hydropower plants account for approximately 86% of global hydropower production and are defined as facilities with a power capacity exceeding 10 MW. Conversely, small-scale hydropower plants (8.3%) encompass all installations below this threshold. This latter category, increasingly adopted for electricity generation, is further subdivided into small, mini, and micro hydropower plants [12].

In practical terms, small-scale hydropower installations exhibit minimal differences from large-scale plants, with the primary distinction lying in their simplified design and operation [13]. These installations are cost-effective, can work automatically without permanent personnel, and require minimal supervision and maintenance downtime. Typically, they operate as run-of-river systems, eliminating the need for costly accumulation reservoirs, which are economically unfeasible for smaller facilities [14, 15].

Four key parameters define the importance of hydropower development:

- Design flow rate: The maximum water discharge that the turbine can process
- Head height: The elevation difference utilized for power generation
- Installed power capacity: The rated power output of the plant
- Electricity production: The total energy output over time.

Beyond these parameters, micro-hydropower plants are classified based on their water intake method, the manner in which water is conveyed to the turbine, and the turbine's physical placement within the system.

There are two primary classifications of micro-hydropower plants: used on: low-pressure, medium and high-pressure. Low-pressure installations are located along a river or on a diversion canal. The most critical infrastructure is the dam or intake structure, typically constructed of concrete. Its primary function is to divert the required water flow directly to the turbine or into a diversion canal while allowing floodwaters to pass. The power plant can be integrated directly into the dam or located at the end of a channel.

Generally, there is no penstock, or it remains very short. The head heights for these installations range from 2 to 20 meters, and the turbine operates under low pressure. Medium-pressure and high-pressure installations are situated on rivers, mountain streams, potable water networks, and industrial hydraulic circuits. Low-pressure installations have a penstock localed between the intake and the power plant. This pressurized channel is the most crucial component of this type of mini-hydropower plant. Hydraulic turbines used in micro-hydropower plants are categorized into two primary groups, as illustrated in Figure 1

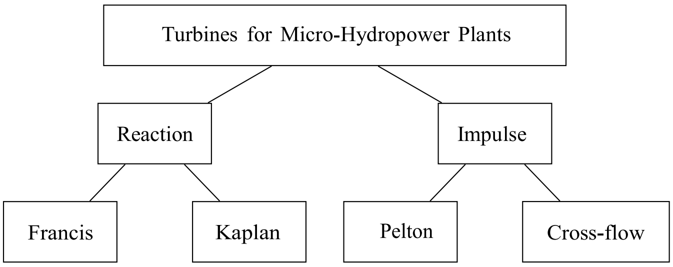

Figure 1. Classification of hydraulic turbines used in micro-hydropower plants

3. Turbines Runner Selection Criteria

Basically, a significant factor in selecting a micro-hydraulic turbine is its relative efficiency, which varies according to the design point depends on operational conditions such as head height and flow rate. Each turbine type possesses a distinct optimal efficiency for given conditions, as illustrated in Figure 2 [16], providing guidance for the selection of the most suitable turbine.

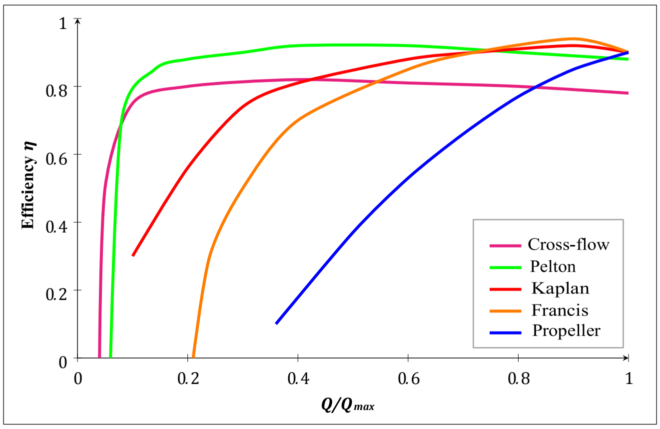

Figure 2. Part flow efficiencies

The fundamental equation governing any hydroelectric system is expressed as follows:

$$P_s = \eta \rho g Q H \tag{1}$$

where, *Ps* is the mechanical power produced at the turbine shaft (watts), η the hydraulic efficiency of the turbine, ρ the density of water volume (kg/m^3), g the acceleration due to gravity (m/s^2), *Q* the flow rate passing through the turbine (m^3/s), and H the effective pressure head of water across the turbine (m).

In addition, the selection of turbines also depends on multiple criteria including shaft speed, and specific speed as illustrated in Table 1 [17]. Additional factors must also be considered, such as the optimal depth for turbine placement, its overall performance, and cost-effectiveness [18]. Williamson et al. [18] proposed a methodology for selecting the most efficient turbine for a given application, optimizing both energy output and economic viability. Each turbine type exhibits a specific efficiency at different heads and partial flows.

Table 1. Range of selection [18]

Quantitative criteria	**Qualitative criteria**
Rated flow/head efficiency	Environmental - weather - location
Part flow/head efficiency	Required civil works
Cost	Portability
Turbine rotational speed	Maintainability
Power for given site	Reliability
Size of system	Ease of manufacture

Pressure head height is a fundamental criterion in the classification of hydropower turbines, distinguishing them into high-head, medium-head, and low-head categories, as outlined in Table II. For micro-hydropower systems, the selected turbines are typically designed for heads less than 10 meters.

Table 2. Small hydropower applications turbines head classification [19]

Turbine types	Head classification		
	(High > 50 m)	**(Medium 10-15 m)**	**(Low < 10 m)**
Impulse	Pelton	Cross flow	Cross flow
	Turgo	Turgo	
	Multi-jet Pelton	Multi-jet Pelton	
		Francis (spiral case)	
Reaction			Francis
			Propeller
			Kaplan

However, larger hydropower turbines can be adapted for micro-hydropower applications through specific modifications to enhance their suitability. In the medium-head range, pumps-as-turbines (PATs) have emerged as a viable solution, demonstrating cost-effectiveness and operational efficiency.

Figures 3 and 4 [19], further illustrate the optimal operating ranges (Head vs. Flow) for different turbine types, positioning the Cross-flow turbine as ideal for low-head and moderate-flow micro-hydropower sites.

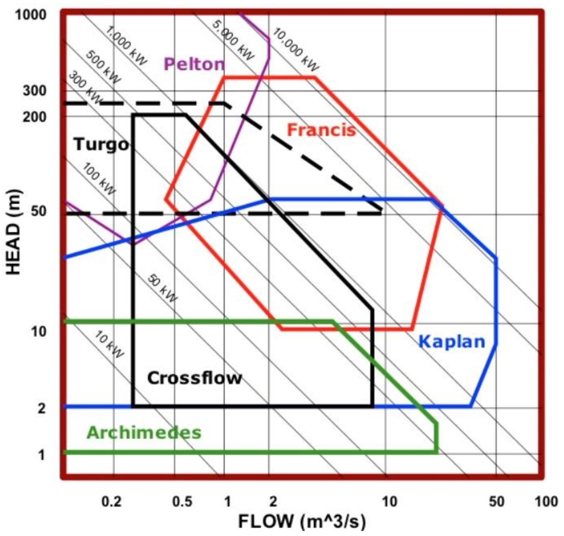

Figure 3. Various turbines in terms of head and flow rate

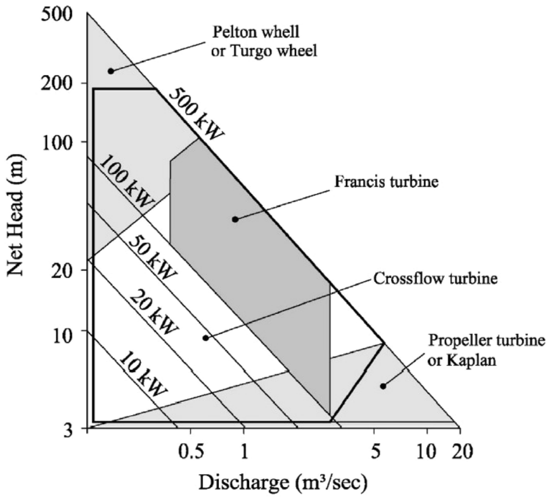

Figure 4. The range of selection of small and microhydroturbines with heads and flow rates variations

Another critical parameter influencing turbine operation is the specific speed [19], which serves as a dimensionless indicator of a turbine's performance. Specific speed establishes a relationship between the turbine's output power, rotational speed, and hydraulic head, as expressed in Equation 2:

$$N_s = \frac{nP_s^{0.5}}{H^{5/4}} \tag{2}$$

where, n is the turbine speed (rpm) and H denotes the pressure head across the turbine (m). The maximum hydraulic efficiency is approximately 80% [20], and it is defined as the ratio of power output to power input:

$$\eta = \frac{P_{out}}{P_{in}} = \frac{M\omega}{\rho g H_n Q} \ [\%] \tag{3}$$

where, M is the shaft torque [Nm], ω is the runner angular velocity [rad/s], ρ is the water density [kg/m^3], g is the acceleration of gravity [9.81 m/s^2], Q is the flow rate [m^3/s]. The net head Hn can be approximately calculated as 0.94H where H is the gross head [21].

The selection of installation sites plays a critical role in determining the hydropower potential that micro-turbine systems can harness. Adhau et al. [22] conducted a comprehensive multi-site evaluation using hydrological data to assess the feasibility of mini- and micro-hydropower plants. Their findings indicate that hydropower facilities integrated into irrigation networks can reliably generate electricity that meets both technical standards and local energy demands at affordable costs. Moreover, the energy potential of micro-hydropower plants is significantly enhanced when utilizing irrigation canal heads with higher elevations, compared to systems relying solely on high flow rates [23]. These results underscore the necessity of optimizing turbine selection according to site-specific conditions, as this directly influences operational performance and long-term sustainability [24].

4. Materials and Manufacturing Methodology

The research methodology is structured into three sequential stages: (1) design, (2) manufacturing, and (3) validation. This section provides a detailed description of the manufacturing process as well as the material behavior laws that govern the performance of the selected thermoplastic.

4.1. Thermoforming Process

Thermoforming is a polymer shaping technique where a thermoplastic sheet is heated until pliable and then formed over a mold [25]. Thermoforming by molding has become one of the leading processes for shaping thermoplastic polymers. Several thermoforming techniques are commonly employed, including:

- Contact molding;
- Punch-die molding;
- Vacuum or pressure forming;
- Injection molding;
- Stamping forming (primarily used for thermoplastic matrix composites).

For this study, the stamping thermoforming method was selected for blade fabrication due to its compatibility with HDPE, ease of use, and the availability of equipment in our laboratory. The general process is illustrated in Figure 5.

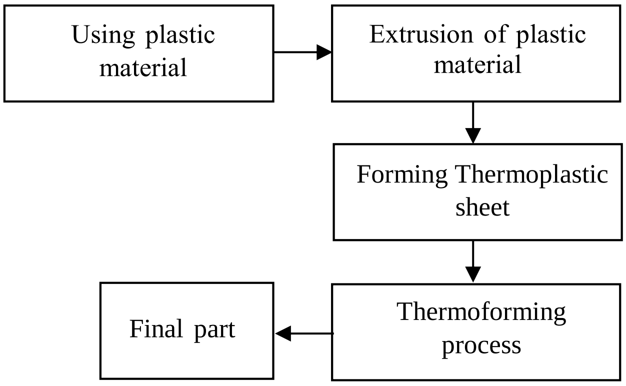

Figure 5. Process of obtaining a thermoplastic sheet

This process, detailed in Figure 6 [25], involves steps from impregnation to finishing. The thermal cycle in Figure 7 is reversible, highlighting that thermoplastics like HDPE [26, 27] are recyclable materials. The specific parameters used for HDPE in this study, including an inflation temperature range of 130-150°C, are detailed in Table 3.

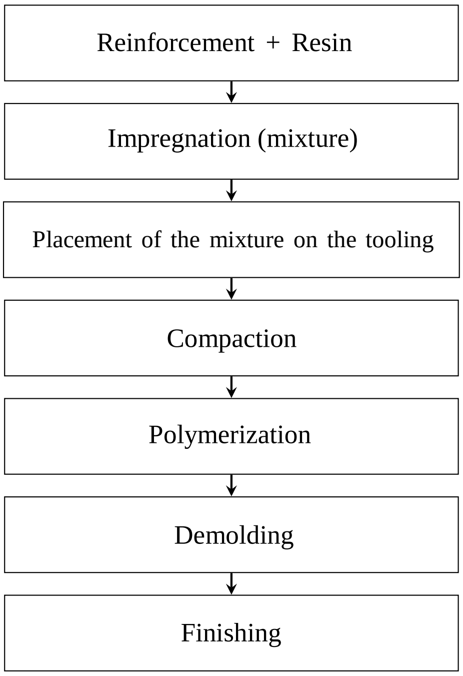

Figure 6. Thermoforming process steps

Table 3. Pressure and temperature ranges for different polymers [28]

Polymer	Pressure interval/inflation (kPa)	Temperature Interval Inflation (°C)
HDPE	7-21	130-150

The thermal loading cycle of the oven, illustrated in Figure 7, can be divided into four distinct stages. The corresponding pressure and temperature ranges remain consistent with the principles of the ideal gas law. Importantly, the process is fully reversible a defining characteristic of thermoplastics which enables their recyclability and repeated processing without significant degradation [29].

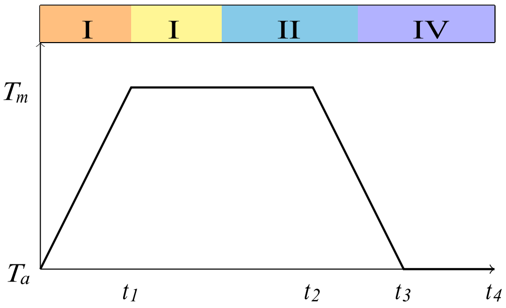

Figure 7. Thermoforming cycle [28]

4.2. Behavioral Laws

Laws of Biocomposites are characterized by the viscoelastic model for thermoplastic materials and are modeled here using the finite element method. The integral model of Lodge for linear viscoelasticity and the K-BKZ model for nonlinear viscoelasticity are used for characterization [30, 31]. Characteristics of the Lodge viscoelastic model is given in Equation 4 [32]:

$$[\sigma(t)] = -p[I] + \int_{-\infty}^{t} \mu(t-t')[c(t,t')^{-1}]'dt' = 0 \tag{4}$$

where, p is the hydrostatic pressure, $[I]$ is the identity matrix and $[c(t,t')]$ is the deformation tensor, defined in Equation 5:

$$[c(t,t')] = [F(t')]^{-T}[c(t)][F(t')]^{-T} \tag{5}$$

where, $[c(t,t')]$ is the Finger tensor, and μ is the memory function.

Regarding the memory function, it is given by:

$$\mu(t,\tau)=\sum_k \frac{g_k e^{-\frac{(t-\tau)}{\tau_k}}}{\tau_k} \tag{6}$$

where, τ_k represents the relaxation time associated with the stiffness g_k.

The shear stress $\sigma_{xy}(t)$ for the Lodge model is:

$$[\sigma_{xy}(t)]=\int_{-\infty}^{t}\sum_k \frac{g_k e^{-\frac{(t-\tau)}{\tau_k}}}{\tau_k}\big(\gamma(t')-\gamma(t)\big)d\tau \tag{7}$$

Heat modeling is performed using the Ritz-Galerkin approach. The method consists of using the interpolation functions $V(x)$ as test functions N_j for the temperature field T [33, 34].

$$T(\xi,\eta,\zeta,t)=\sum_{j=1}^{m} T_j^e(t)N_j^e(\xi,\eta,\zeta) \tag{8}$$

where, m is the number of nodes, $T_j^e(t)$ the nodal values of the temperature t, $N_j(\xi,\eta,\zeta)$ isoparametric interpolation function and (ξ,η,ζ) nodal coordinates.

4.3. Liquid Flow Equations in a Cross-flow Turbine

Given the complexity of analytically solving the Navier-Stokes and continuity equations, this study relies on AnsysCFD and Ansys-Static software, which offer advanced numerical capabilities for the precise simulation of fluid dynamics and structural analyses.

Several assumptions are considered in this study as at:

- The liquid is considered incompressible;
- The flow is considered steady-state : the components are time-independent ;
- The liquid is considered Newtonian ;
- The energy conservation equations are not considered: the temperature is constant (no degradation of mechanical energy into thermal energy).

A. Continuity Equations

The continuity equation for an incompressible fluid, the conservation of mass is:

$$\nabla\cdot(\rho U)=0 \tag{9}$$

where, U represents the velocity of the fluid particle. In Cartesian coordinates, this equation becomes:

$$\frac{\partial u}{\partial x}+\frac{\partial v}{\partial y}+\frac{\partial w}{\partial z}=0 \tag{10}$$

B. Navier-Stokes Equations

They can be written in the terms described below:

$$\nabla\cdot(\rho U\otimes U)=\nabla\cdot(-pI+\mu_{\text{eff}}(\nabla U+(\nabla U)^T))+S_M \tag{11}$$

where, U is velocity, p is pressure, μ_{eff} is effective viscosity, and S_M is the source term for the rotating frame of reference (accounting for centripetal and Coriolis accelerations).

$$S_M=-\rho\big(2\omega\times U+\omega\times(\omega\times r)\big) \tag{12}$$

where, r is the position vector, $2\omega\times U$ represents the centripetal acceleration, and $\omega\times(\omega\times r)$ represents the Coriolis acceleration.

The Navier-Stokes equations in Cartesian coordinates are given by:

$$\rho\left(u\frac{\partial v}{\partial x}+v\frac{\partial v}{\partial y}+w\frac{\partial v}{\partial z}\right)=-\frac{\partial p}{\partial y}+\rho g_y+\mu_{\text{eff}}\left(\frac{\partial^2 v}{\partial x^2}+\frac{\partial^2 v}{\partial y^2}+\frac{\partial^2 v}{\partial z^2}\right)+S_{My} \tag{13}$$

$$\rho\left(u\frac{\partial w}{\partial x}+v\frac{\partial w}{\partial y}+w\frac{\partial w}{\partial z}\right)=-\frac{\partial p}{\partial z}+\rho g_z+\mu_{\text{eff}}\left(\frac{\partial^2 w}{\partial x^2}+\frac{\partial^2 w}{\partial y^2}+\frac{\partial^2 w}{\partial z^2}\right)+S_{Mz} \tag{14}$$

$$\rho\left(u\frac{\partial w}{\partial x}+v\frac{\partial w}{\partial y}+w\frac{\partial w}{\partial z}\right)=-\frac{\partial p}{\partial z}+\rho g_z+\mu_{\text{eff}}\left(\frac{\partial^2 w}{\partial x^2}+\frac{\partial^2 w}{\partial y^2}+\frac{\partial^2 w}{\partial z^2}\right)+S_{Mz} \tag{15}$$

For a constant rotational speed ω along z, the source terms S_{Mx}, S_{My}, and S_{Mz} of the flow are expressed respectively as:

$$S_{Mx} = \rho(\omega_z^2 r_x + 2\omega_z v) \tag{16}$$

$$S_{My} = \rho(\omega_z^2 r_y - 2\omega_z u) \tag{17}$$

$$S_{MZ} = 0 \tag{18}$$

C. Equilibrium Equations

In terms of normal and shear stresses, they are written as:

$$\begin{cases} \partial\sigma_{\mathrm{x}}/\partial x + \partial\tau_{\mathrm{x}\gamma}/\partial y + \partial\tau_{\mathrm{x}}z/\partial z + F_{\mathrm{x}} = 0 \\ \partial\tau_{\gamma\mathrm{x}}/\partial x + \partial\sigma_{\gamma}/\partial y + \partial\tau_{\gamma}z/\partial z + F_{\gamma} = 0 \\ \partial\tau z_{\mathrm{x}}/\partial x + \partial\tau z_{\gamma}/\partial y + \partial\sigma z/\partial z + Fz = 0 \end{cases} \tag{19}$$

where, F_x,F_y,F_z are the components of the forces per unit volume.

D. Strain-Displacement Equations

They are given by the following relations:

$$\begin{cases} \varepsilon_{\mathrm{x}} \ = \ \partial u/\partial x \\ \varepsilon_{\gamma} \ = \ \partial v/\partial y \\ \varepsilon z \ = \ \partial w/\partial z \end{cases} \tag{20}$$

$$\begin{cases} \gamma_{\mathrm{x}\gamma} = \partial u/\partial y + \partial v/\partial x \\ \gamma_{\gamma}z = \partial v/\partial z + \partial w/\partial y \\ \gamma z_{\mathrm{x}} = \partial w/\partial x + \partial u/\partial z \end{cases} \tag{21}$$

E. Stress-Strain Equations

$$\begin{cases} \varepsilon_{\mathrm{x}} = \sigma_{\mathrm{x}}/E - \nu\cdot\sigma_{\gamma}/E - \nu\cdot\sigma_Z/E \\ \varepsilon_{\gamma} = \sigma_{\gamma}/E - \nu\cdot\sigma_Z/E - \nu\cdot\sigma_{\mathrm{x}}/E \\ \varepsilon_Z = \sigma_Z/E - \nu\cdot\sigma_{\mathrm{x}}/E - \nu\cdot\sigma_{\gamma}/E \\ \gamma_{\mathrm{x}\gamma} = \tau_{\mathrm{x}\gamma}/G \\ \gamma_{yz} = \tau_{yz}/G \\ \gamma_{zx} = \tau_{zx}/G \end{cases} \tag{22}$$

The primary criterion used to determine failure is based on the von Mises stress, which is given by:

$$\sigma' = \sqrt{\frac{1}{2}((\sigma_1 - \sigma_2)^2 + (\sigma_2 - \sigma_3)^2 + (\sigma_3 - \sigma_1)^2)} \tag{23}$$

where, σ_1,σ_2,σ_3 are the principal stresses defined in Equations 24, 25 and 26 respectively.

$$\sigma_1 = \sigma_0 + 2\left(\left|\frac{J_2}{3}\right|\right)^{1/2} \cos\left(\frac{1}{3}\arccos\left(0.5 J_3 \left|\frac{J_2}{3}\right|^{-1.5}\right)\right) \tag{24}$$

$$\sigma_2 = \sigma_0 - 2\left(\left|\frac{J_2}{3}\right|\right)^{1/2} \cos\left(\frac{1}{3}\arccos\left(0.5 J_3 \left|\frac{J_2}{3}\right|^{-1.5}\right) + \frac{\pi}{3}\right) \tag{25}$$

$$\sigma_3 = \sigma_0 - 2\left(\left|\frac{J_2}{3}\right|\right)^{1/2} \cos\left(\frac{1}{3}\arccos\left(0.5 J_3 \left|\frac{J_2}{3}\right|^{-1.5}\right) - \frac{\pi}{3}\right) \tag{26}$$

where:

$\sigma_0 = \frac{1}{3}(\sigma_x + \sigma_y + \sigma_z)$

$J_2 = S_x S_y + S_y S_z + S_z S_x - \tau_{xy}^2 - \tau_{yz}^2 - \tau_{zx}^2$

$J_3 = -(S_x S_y S_z - S_x \tau_{yz}^2 - S_y \tau_{zx}^2 - S_z \tau_{yx}^2)$

$S_x = \sigma_x - \sigma_0$

$S_y = \sigma_y - \sigma_0$

$S_z = \sigma_z - \sigma_0$

The von Mises safety factor S_F given in Equation 27.

$$S_F = \frac{S_y}{\sigma'} \tag{27}$$

where, S_x, S_y, S_t is the yield strength of the material in three dimensions.

5. Turbine Design Parameters

The mechanical properties of the HDPE used in the simulation, contrasted with S235 Steel, are presented in Table 4.

Table 4. Mechanical properties of S235 Steel and HDPE [34]

Material Properties	S235 Steel	HDPE
Density ρ [kg/m^3]	7800	950
Young's Modulus E [Pa]	210×10^9	0.8×10^9
Poisson's Ratio v	0.3	0.4
Bulk Modulus K [Pa]	160×10^9	66.7×10^6
Shear Modulus G_c [Pa]	8×10^{10}	3.75×10^8
Yield Strength R_e [Pa]	235×10^6	22×10^6
Melting Temperature [°C]	1450	130
Thermal Conductivity k [W/mK]	30	0.4
Tensile Strength R_m [Pa]	7.446×10^8	28×10^6
Specific Heat Capacity C_p [J/kgK]	460	1900

The turbine geometry was designed using Autodesk Inventor 2024 in Figure 8. The runner design was based on the parameters of the laboratory's HT-703 Multi Turbine Test Set, with a rotational speed (N) of 428 rpm, a flow rate (Q) of 24 m³/h, and 15 blades (Z).

Figure 8. Solid model of the Cross-flow turbine

The sizing of a Cross-flow turbine depends on site data as defined below:

a) Net Head Height H_n

$$H_n = H_g - H_{tl} \tag{28}$$

where, H_n is the net head (m), representing the actual available head at the turbine after accounting for losses; H_g is the geometric or gross head (m), measured between the upstream and downstream water levels; H_{tl} is the total head loss is (≈ 7% of H_g) (m) [35], (including energy losses due to friction and turbulence in the conduits).

b) Flow Rate Q

$$Q = V_r \cdot A_r \tag{29}$$

where, Q is the volumetric flow rate (m^3/s); V_r is the mean relative velocity (m/s); A_r is the effective passage area perpendicular to the velocity V_r (m^2).

c) Specific Speed of the Turbine N_s

$$N_s = \frac{513.25}{H_n^{0.505}} \tag{30}$$

d) Rotational Speed of the Turbine N

$$N = 513.25 \cdot \frac{H_n^{0.745}}{\sqrt{P_a}} \tag{31}$$

e) Outer Diameter of the Wheel D_1

$$D_1 = \frac{40 \cdot k}{H_n/N} \tag{32}$$

f) Blade Thickness e

$$e = 0.326 R_1 \tag{33}$$

g) Number of Blades n

$$n = \frac{\pi D_1}{e} \tag{34}$$

To design a Cross-flow turbine blade, it is essential to define its geometry based on hydraulic principles and velocity triangles [36, 37]. The critical geometrical parameters, illustrated in Figure 9 [38, 39], were determined using established hydraulic equations. Key parameters include the runner's outer radius R_1, inner radius $R_2 = 0.66\ R_1$ [39]. inlet angle $\alpha_1 = 16^\circ$, outer blade angle $\beta_1 = 30^\circ$, and inner blade angle $\beta_2 = 90^\circ$. The blade angles are characterized by the incidence angle (also referred to as the angle of attack), which specifies the blade orientation relative to the incoming flow. Additional parameters defining the blade profile include the curvature radius r_b, the pitch circle radius r_p, and the blade segment angle δ [40].

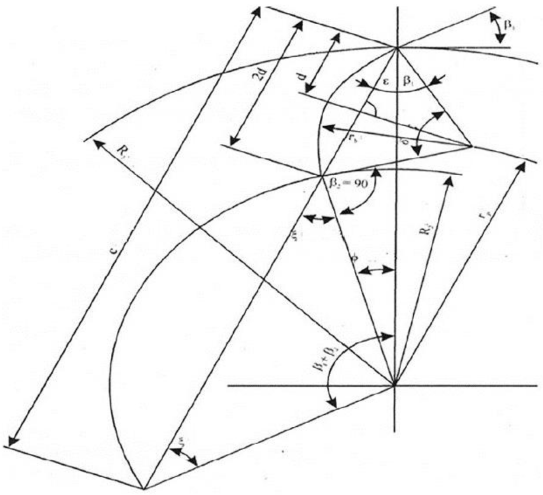

Figure 9. Blade profile of a Cross-flow turbine runner [37]

$$C = \sqrt{R_1^2 + R_2^2 - 2R_1R_2\cos(\beta_1 + \beta_2)} \tag{35}$$

$$\varepsilon = \arcsin\left(\frac{R_2\sin(\beta_1+\beta_2)}{C}\right) \tag{36}$$

$$\xi = 180^\circ - (\beta_1 + \beta_2 + \varepsilon) \tag{37}$$

$$\varphi = (\beta_1 + \beta_2) - (180^\circ - 2\xi) \tag{38}$$

$$d = R_1 sin(\varphi)/[2sin(180^\circ - \xi)] = 180^\circ - 2(\beta_1 + \varepsilon) \tag{39}$$

$$r_b = \frac{d}{cos(\beta_1+\varepsilon)} \tag{40}$$

$$r_p = \sqrt{({r_b}^2 + {R_1}^2 - 2 \cdot r_b \cdot R_1 \cdot cos(\beta_1))} \tag{41}$$

This digital design was subsequently used to manufacture the physical HDPE prototype, which is presented in Figure 10.

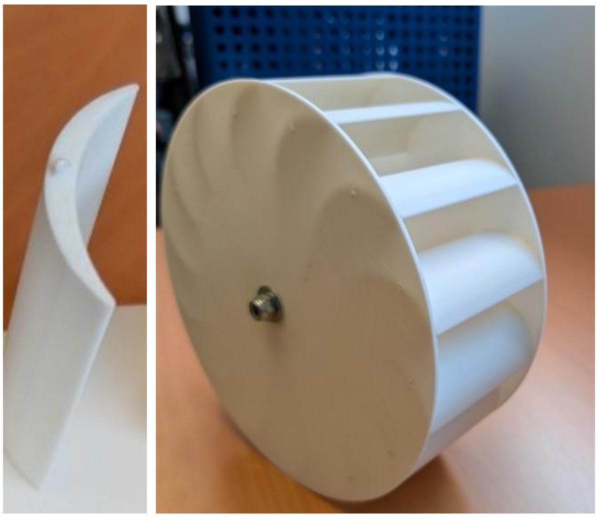

(a) Blade **(b) Overall view of the Cross-flow runner**

Figure 10. Prototype of the Cross-flow wheel in HDPE

6. Simulation Process

Solving the complete fluid flow equations analytically is impractical. Consequently, this study employs ANSYS-CFD to perform fluid dynamics simulations and ANSYS-Static to conduct structural analyses. The integrated solution framework is depicted in Figure 11.

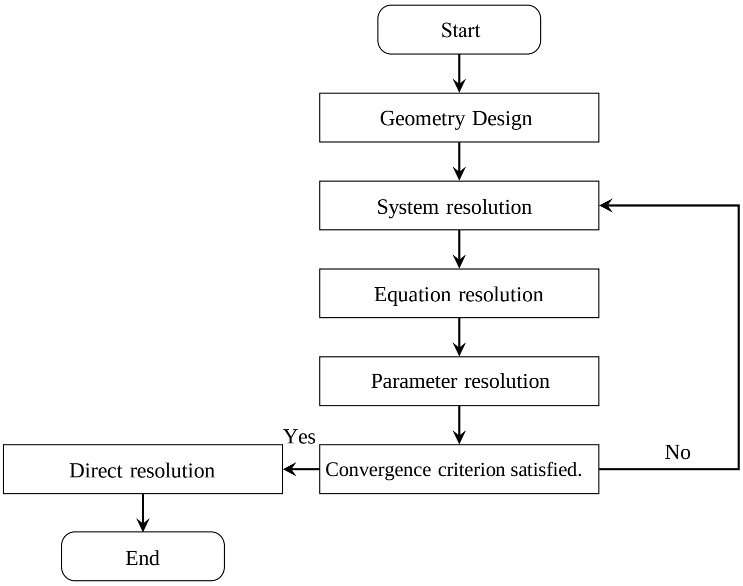

Figure 11. Solution Framework of the ANSYS-CFX Code

The numerical simulations were conducted using the $k - \epsilon$ turbulence model to capture the effects of turbulent flow behavior. Boundary conditions were specified as a static pressure at the inlet and a prescribed mass flow rate at the outlet. To accurately resolve near-wall phenomena, the wall function approach was adopted. Furthermore, the rotor-stator interaction was modeled using the Frozen-Rotor interface condition, ensuring a steady-state approximation of relative motion between rotating and stationary domains.

A mesh sensitivity analysis was performed to verify the independence of the numerical results from grid resolution. Two mesh configurations were evaluated: a coarse mesh consisting of 10,721 elements and a refined mesh comprising 23,352 elements. The comparison revealed a notable deviation of 13.39% in key performance indicators, such as torque and hydraulic efficiency. Given this discrepancy, the refined mesh was selected for all subsequent simulations to ensure numerical accuracy and solution convergence. This approach aligns with the findings of recent studies, such as the work by Galvis-Holguin et al., who demonstrated that mesh refinement significantly improves the reliability of CFD predictions in turbine design, particularly in the context of Michel-Banki turbines [41, 42, 43].

A 2D fluid domain was generated and meshed using ANSYS 2024-R1 (Figure12). A mesh refinement zone was implemented around the rotor blades to accurately capture the fluid-structure interactions and resolve high-velocity and pressure gradients, which is essential for reliable simulation results.

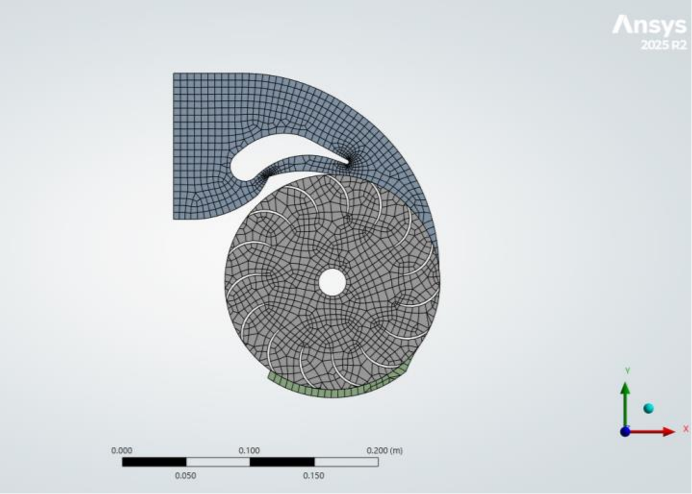

Figure 12. Mesh of the Cross-flow turbine fluid model

This refinement allows for better resolution of fluid-structure interactions and local variations in pressure and velocity. Conversely, the use of an overly coarse mesh can induce numerical errors, potentially undermining the reliability and validity of the simulation results.

To replicate the experimental conditions, boundary conditions were carefully defined within the simulation domain. A pressure inlet of 100000 Pa was applied at the upstream boundary, while a mass flow outlet of 3 kg/s was prescribed at the downstream end. The turbine runner was modeled as a rotating domain operating at 428 rpm, with a no-slip condition imposed on all blade surfaces to capture viscous effects. The surrounding turbine housing was treated as a stationary no-slip wall, ensuring representation of fluid-structure interactions and confinement effects

7. Results and Discussion

This section presents the results of the numerical simulations (CFD and FEA) together with the experimental validation, providing a comparative assessment of the HDPE runner against a conventional steel runner.

7.1. Hydrodynamic Simulation (CFD)

The CFD simulation provides detailed insights into the fluid dynamics of the system. Figure 13 illustrates the velocity contours, where a significant acceleration of the fluid is observed as it passes through the nozzle and impinges on the blades. The velocity distribution across the blade surfaces is heterogeneous a typical characteristic of Cross-flow turbines. Elevated velocities in the peripheral region further indicate efficient conversion of kinetic energy into mechanical work.

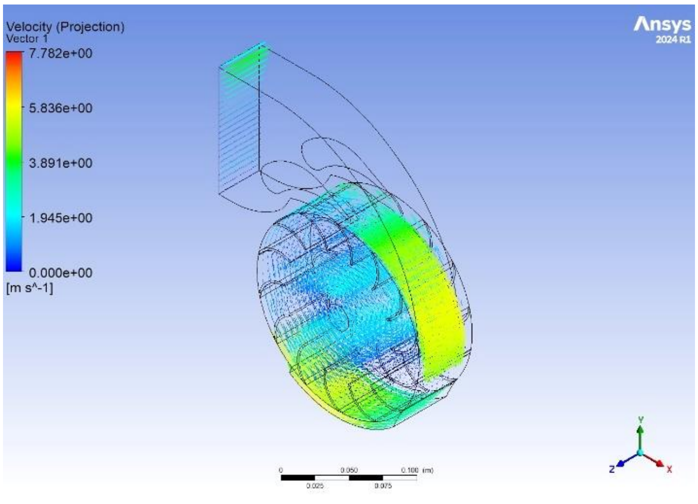

Figure 13. Velocity Contour

Figure 14 illustrates the pressure distribution. The pressure is highest at the inlet (stagnation point) and progressively decreases as the fluid flows through the runner, transferring its energy. The isobars clearly demonstrate the double-pass flow (a hallmark of Cross-flow turbines) where the fluid traverses the upper blades and subsequently passes through the lower blades before exiting. The significant pressure gradients observed are associated with turbulence, which directly influences turbine efficiency.

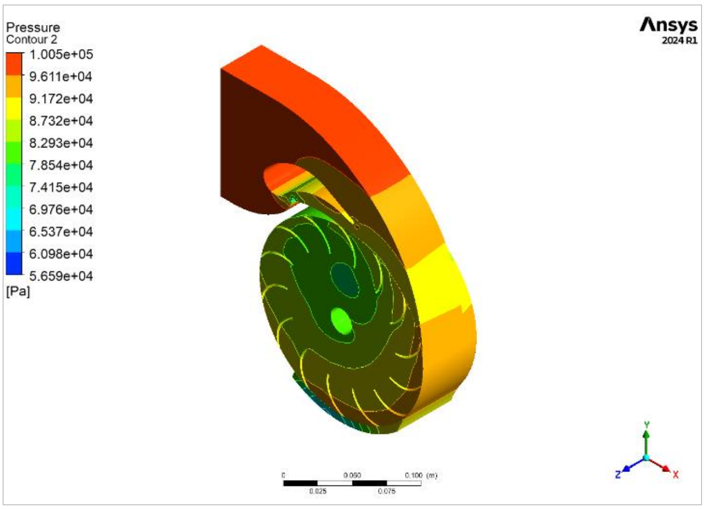

Figure 14. Pressure Contour

7.2. Performance Comparison: HDPE vs. Steel

The primary objective of this study was to compare the performance of the HDPE runner with that of a conventional steel runner using an identical design. Figure 15 presents the turbine efficiency as a function of flow rate. The results indicate that the HDPE runner (both numerical and experimental) achieves between 80% and 83% of the efficiency obtained with the steel runner. This performance gap is primarily attributed to the lower stiffness (Young's modulus) of HDPE, which can cause minor blade deformations under hydrodynamic loading, thereby slightly modifying the blade's optimal angle of attack.

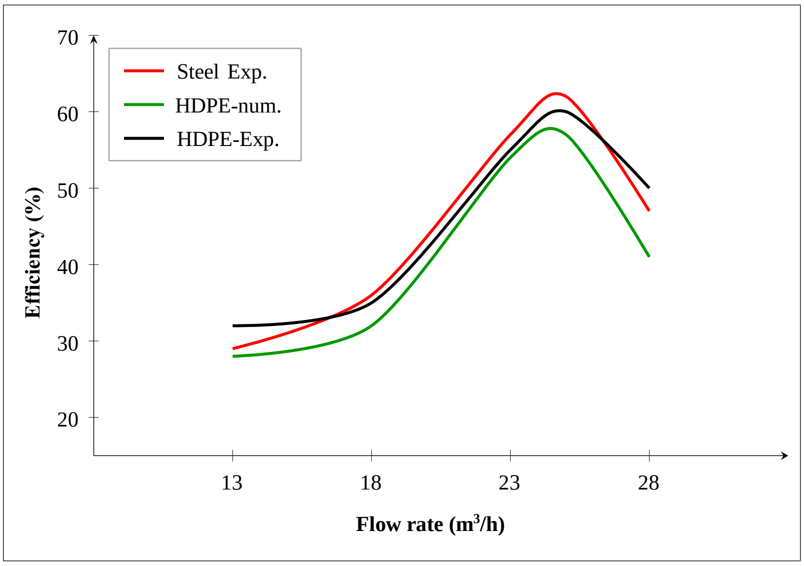

Figure 15. Efficiency of Cross-flow turbine Steel vs HDPE

Figure 16 compares the mechanical shaft power. In contrast to efficiency, the steel runner does not demonstrate a significant advantage over the HDPE runner; the power output curves are nearly identical. This indicates that HDPE provides comparable energy transmission. Figure 17 further confirms this, showing that the HDPE runner demonstrates performance comparable to steel across a wide range of rotational speeds.

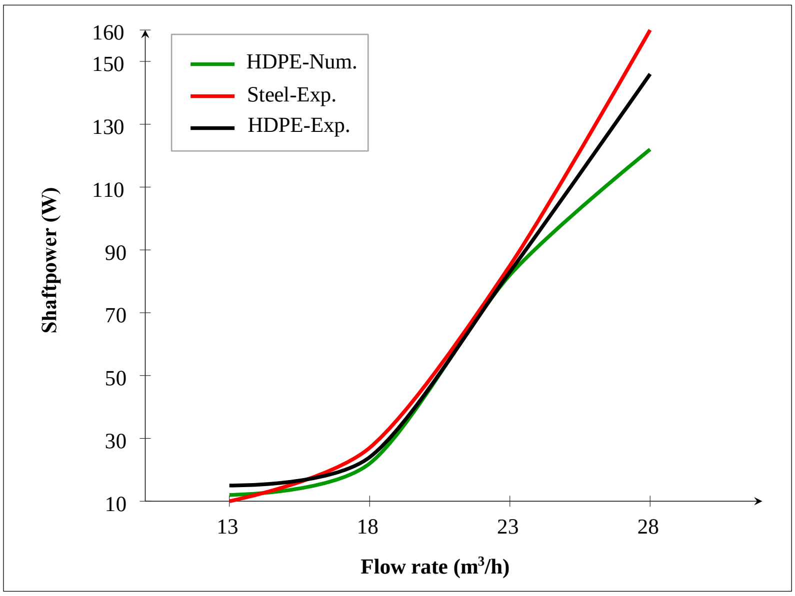

Figure 16. Comparison of mechanical power between steel and HDPE blades of the Cross-flow turbine

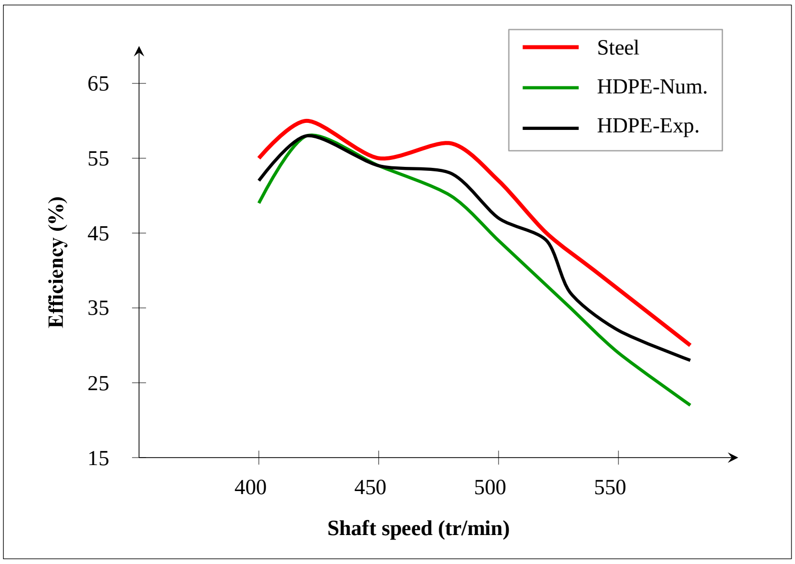

Figure 17. Efficiency as a function of rotational speed

7.3. Comparison with Previous Studies

The performance observed in this study is consistent with findings in the broader literature. Typical efficiencies for non-optimized Cross-flow turbines are often reported in the 70-85% range. Recent 2025 studies validating new Cross-flow designs through similar CFD and experimental methods reported peak efficiencies of 80.36%. Other experimental investigations have demonstrated that well-designed Cross-flow turbines can achieve peak efficiencies of 84.8%, with highly optimized research designs reaching 88-90% [14, 44, 45].

Our finding that the HDPE runner achieves 80-83% of the steel runner's efficiency places its performance squarely within the expected range for this type of turbine. This confirms that the use of HDPE, while resulting in a minor efficiency reduction compared to rigid steel, delivers a viable and competitive alternative rather than a drastic performance loss.

7.4. Structural Analysis (FEA) and Validation

The hydrodynamic pressure and forces calculated by the CFD were applied as loads in the FEA (ANSYS-Static) to evaluate the structural integrity of the HDPE runner. Figure 18 shows the von Mises stress as a function of flow rate. Stresses increase linearly, reaching a peak of approximately 8.5 MPa at the maximum flow rate (28 m^3/h). This maximum stress is well below HDPE's yield strength of 22 MPa (from Table 4), indicating a significant safety factor of approximately 2.6

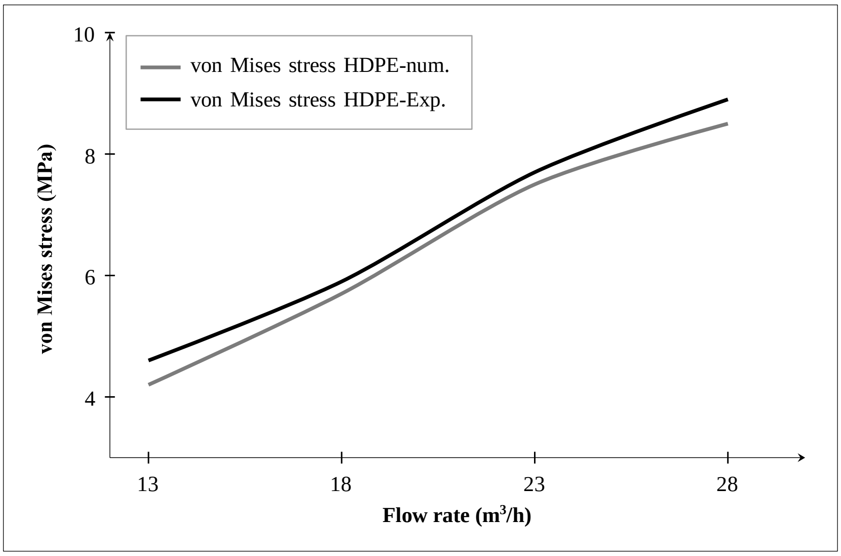

Figure 18. Variation of von Mises stress as a function of flow rate for HDPE blades

Figures 19 and 20 illustrate the radial and axial forces, respectively. Both forces exhibit a moderate and progressive increase with the flow rate, confirming that the loads on bearings and supports remain relatively low. This behavior highlights one of the advantages of the lightweight HDPE design.

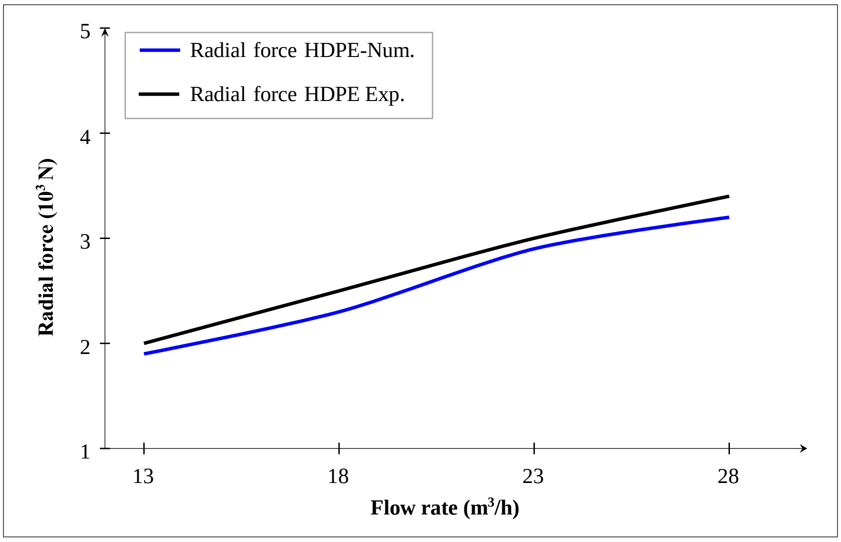

Figure 19. Variation of radial force as a function of flow rate for HDPE blades

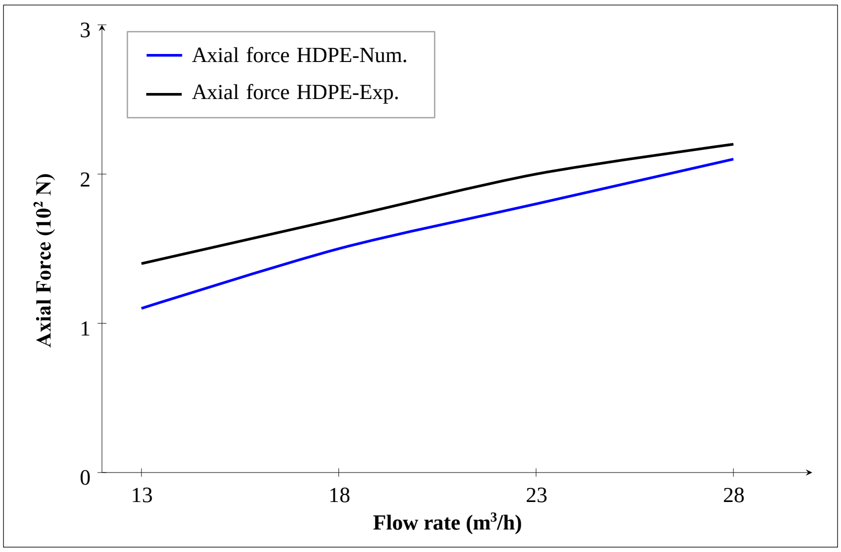

Figure 20. Axial force vs. Flow rate for HDPE blade in a Cross-flow turbine

Finally, Figure 21 illustrates the blade deformation. The deformation (8×10^{-3} mm) is minimal, with a maximum value of approximately 12×10^{-3} mm. This low and controlled deformation confirms that HDPE can efficiently withstand the mechanical loads without compromising the runner's design under the given operational conditions.

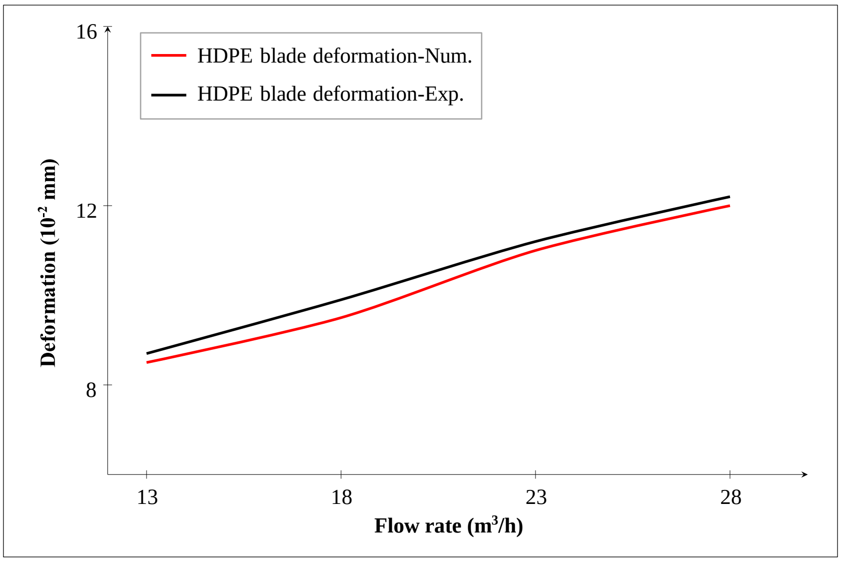

Figure 21. Deformation vs. Flow rate for HDPE blade in a Cross-flow turbine

7.5. Discussion of Discrepancies and Limitations

Across Figures 15, 18, 19, 20, and 21, a small but consistent discrepancy is observed between the numerical (CFD and FEA) and experimental results. In general, the experimental data indicate slightly lower efficiency and stress values compared to numerical predictions. An analysis of the deviation between the two datasets revealed a Root Mean Square Error (RMSE) of 3.8%, confirming a strong correlation between the numerical model and the experimental measurements while highlighting the presence of minor systematic differences.

These discrepancies can be attributed to several idealizations inherent in the numerical model. Effects such as bearing friction, shaft seal drag, and small-scale manufacturing imperfections in the HDPE prototype are not captured in the simulations. In addition, the current model does not incorporate temperature-dependent viscoelastic deformation. Since the experimental validation was conducted under constant laboratory conditions, without varying the operating temperature, slight thermal softening of HDPE under load may have contributed to the observed differences in performance, particularly in terms of blade deformation and efficiency.

Finally, while the present study focuses on micro-hydropower applications, the scalability of the design to medium-power systems requires further investigation. In particular, the impact of increased hydrodynamic forces on long-term deformation and creep behavior of HDPE must be assessed to ensure structural integrity and efficiency under higher load conditions. Overall, the discrepancies identified remain within acceptable bounds, supporting the reliability of the proposed HDPE runner design and confirming its potential as a sustainable alternative to conventional steel runners in micro-hydropower applications.

8. Conclusion

This study demonstrated the feasibility of using high-density polyethylene (HDPE) as a sustainable alternative to conventional metallic alloys in the design and manufacture of Cross-flow turbine runners for micro-hydropower. By combining numerical simulations (CFD and FEA) with experimental validation, the HDPE runner was shown to achieve 80-83% of the hydraulic efficiency of a steel counterpart while maintaining comparable power output. An analysis of the deviation between numerical and experimental datasets revealed a Root Mean Square Error (RMSE) of 3.8%, confirming the strong correlation between the modeling framework and the physical prototype while highlighting minor systematic differences. Structural analyses further validated the integrity of the runner, with maximum von Mises stresses (8.5 MPa) and blade deformations (0.12mm) remaining well within the material's safety limits under the tested operating conditions.

Beyond technical performance, HDPE offers significant advantages: reduced manufacturing costs, simplified installation due to its lightweight nature, and enhanced durability through superior corrosion resistance. These attributes directly address key barriers to the deployment of micro-hydropower in remote regions, reinforcing HDPE's potential as an economically and environmentally sound solution.

Nevertheless, limitations remain. Long-term fatigue, viscoelastic, and thermal behavior under dynamic loading must be further investigated, and the scalability of the design to medium-power systems requires careful assessment to ensure structural integrity under higher hydrodynamic forces. Future work will also explore HDPE-wood biocomposites, particularly at 40% wood fiber content, to evaluate their durability and performance. Such developments could pave the way for the next generation of cost-effective and sustainable micro-hydropower technologies.

9. Declarations

9.1. Author Contributions

Conceptualization, F.M.K., G.D.N., and F.E.; methodology, F.M.K.; software, F.M.K.; validation, F.M.K., G.D.N., and T.M.T.; formal analysis, F.M.K. and T.M.T.; investigation, F.M.K.; resources, G.D.N. and F.E.; data curation, F.M.K.; writing—original draft preparation, F.M.K.; writing—review and editing, G.D.N., F.E., and T.M.T.; visualization, F.M.K.; supervision, G.D.N. and F.E.; project administration, G.D.N. and F.E. All authors have read and agreed to the published version of the manuscript.

9.2. Data Availability Statement

The data presented in this study are available on request from the corresponding author.

9.3. Funding

The authors received no financial support for the research, authorship, and/or publication of this article.

9.4. Acknowledgments

The authors extend their sincere gratitude to the Laboratory of Turbomachines, the Laboratory of Bioplastics and Nanotechnology, and the Laboratory of Biomaterials at UQAT for their invaluable technical and logistical support.

9.5. Institutional Review Board Statement

Not applicable.

9.6. Informed Consent Statement

Not applicable.

9.7. Declaration of Competing Interest

The authors declare that they have no known competing financial interests or personal relationships that could have appeared to influence the work reported in this paper.

10. References

[1] Business Norway. (2024). Deep river mobile hydropower plants for off-grid areas. Business Norway, Oslo, Norway.

[2] Sen, R., & Bhattacharyya, S. C. (2014). Off-grid electricity generation with renewable energy technologies in India: An application of HOMER. Renewable Energy, 62, 388–398. doi:10.1016/j.renene.2013.07.028.

[3] Elbatran, A. H., Yaakob, O. B., Ahmed, Y. M., & Shabara, H. M. (2015). Operation, performance and economic analysis of low head micro-hydropower turbines for rural and remote areas: A review. Renewable and Sustainable Energy Reviews, 43, 40–50. doi:10.1016/j.rser.2014.11.045.

[4] Assefa, E. Y., & Tesfay, A. H. (2025). Effect of Blade Profile on Flow Characteristics and Efficiency of Cross-Flow Turbines. Energies, 18(12), 3203. doi:10.3390/en18123203.

[5] Harefa, P., Bramantya, M. A., & Waluyo, J. (2025). Numerical Simulation of the Effect of Number of Runner Blades on a Cross-Flow Turbine Performance. Proceedings of the 10th International Conference on Science and Technology (ICST 2024), 11–25. doi:10.2991/978-94-6463-772-4_3.

[6] Hunt, A., Talpey, G., & Polagye, B. (2025). Experimental evaluation of advanced control strategies for high-blockage cross-flow turbine arrays. arXiv preprint arXiv:2507.02194. doi:10.48550/arXiv.2507.02194.

[7] Harvey, A. (1993). Micro-hydro design manual: A guide to small-scale water power schemes. Intermediate Technology Publications, London, United Kingdom.

[8] Ahmad, H., & Rodrigue, D. (2025). Mechanical Recycling of Crosslinked High-Density Polyethylene (xHDPE). Processes, 13(3), 809. doi:10.3390/pr13030809.

[9] MachineMFG. (2025). Polypropylene vs. HDPE: Material differences and comparisons. MachineMFG, Nanjing, China. Available online: https://shop.machinemfg.com/polypropylene-vs-hdpe-material-differences-and-comparisons/ (accessed on November 2025).

[10] Liu, J., Zhao, C., Zhong, S., & Johanning, L. (2025). The Recyclability of Wind Turbine Blade Material, Manufacturing Process, and Recycling Technology. Marine Energy Research, 2(3), 10014–10014. doi:10.70322/mer.2025.10014.

[11] Al-Salem, S. M., Lettieri, P., & Baeyens, J. (2009). Recycling and recovery routes of plastic solid waste (PSW): A review. Waste Management, 29(10), 2625-2643. doi:10.1016/j.wasman.2009.06.004.

[12] Akin, H., Aytac, Z., Ayancik, F., Ozkaya, E., Arioz, E., Celebioglu, K., & Aradag, S. (2013). A CFD aided hydraulic turbine design methodology applied to Francis turbines. International Conference on Power Engineering, Energy and Electrical Drives, 694–699. doi:10.1109/PowerEng.2013.6635694.

[13] Prabowoputra, D. M., Prabowo, A. R., Yaningsih, I., Tjahjana, D. D. D. P., Laksono, F. B., Adiputra, R., & Suryanto, H. (2023). Effect of Blade Angle and Number on the Performance of Bánki Hydro-Turbines: Assessment using CFD and FDA Approaches. Evergreen, 10(1), 519–530. doi:10.5109/6782156.

[14] Popescu, C. (2013). Design and Manufacturing of a Low Head Banki Turbine. Applied Mechanics and Materials, 371, 672-676. doi:10.4028/www.scientific.net/AMM.371.672.

[15] Laghari, J. A., Mokhlis, H., Bakar, A. H. A., & Mohammad, H. (2013). A comprehensive overview of new designs in the hydraulic, electrical equipments and controllers of mini hydro power plants making it cost effective technology. Renewable and Sustainable Energy Reviews, 20, 279-293. doi:10.1016/j.rser.2012.12.002.

[16] Fraenkel, P., Paish, O., Harvey, A., Brown, A., Edwards, R., & Bokalders, V. (1991). Micro-hydro Power. IT Power, Eversley, United Kingdom. Available online: https://www.osti.gov/etdeweb/biblio/5564378 (accessed on November 2025).

[17] Ghosh, T. K., & Prelas, M. A. (2011). Hydropower. In Energy Resources and Systems: Volume 2: Renewable Resources. Springer, Dordrecht, Netherlands. doi:10.1007/978-94-007-1402-1_3.

[18] Williamson, S. J., Stark, B. H., & Booker, J. D. (2014). Low head Pico hydro turbine selection using a multi-criteria analysis. Renewable Energy, 61, 43-50. doi:10.1016/j.renene.2012.06.020.

[19] Paish, O. (2002). Small hydropower: Technology and current status. Renewable and Sustainable Energy Reviews, 6(6), 537–556. doi:10.1016/S1364-0321(02)00006-0.

[20] Anand, R. S., Jawahar, C. P., Bellos, E., & Malmquist, A. (2021). A comprehensive review on Crossflow turbine for hydropower applications. Ocean Engineering, 240(1), 44–44. doi:10.1016/j.oceaneng.2021.110015.

[21] Nasir, B. A. (2013). Design of High Efficiency Cross-Flow Turbine for Hydro-Power Plant. International Journal of Engineering and Advanced Technology, 2(23), 2249–8958.

[22] Adhau, S. P., Moharil, R. M., & Adhau, P. G. (2012). Mini-hydro power generation on existing irrigation projects: Case study of Indian sites. Renewable and Sustainable Energy Reviews, 16(7), 4785-4795. doi:10.1016/j.rser.2012.03.066.

[23] Wang, L., Lee, D. J., Liu, J. H., Chen, Z. Z., Kuo, Z. Y., Lee, W. J., ... & Li, Y. C. (2009, July). A small hydropower (SHP) system in Taiwan using outlet-water energy of a reservoir: System introduction and measured results. IEEE Power & Energy Society General Meeting, 1-7. doi:10.1109/PES.2009.5275958.

[24] Chattha, J. A., Khan, M. S., Wasif, S. T., Ghani, O. A., Zia, M. O., & Hamid, Z. (2010). Design of a cross flow turbine for a micro-hydro power application. American Society of Mechanical Engineers, Power Division (Publication) POWER, 49354, 637–644. doi:10.1115/POWER2010-27184.

[25] Gay, D. (1997). Matériaux composites. Hermès, Paris.

[26] Andoh, P. Y., Sekyere, C. K. K., Ayetor, G. K. K., & Sackey, M. N. (2021). Fabrication and Testing of a Low-Cost Wind Turbine Blade Using Bamboo Reinforced Recycled Plastic. Journal of Applied Engineering and Technological Science, 2(2), 125–138. doi:10.37385/jaets.v2i2.212.

[27] Bilton, K. (2016). Design and fabrication of the trailing edge of a hydraulic turbine blade. Doctoral dissertation, École de technologie supérieure, Montreal, Canada.

[28] Alorchi, T. (2024). Digital investigation on the use of an HDPE and wood-based composite for the manufacture of corrugated sheet metal by thermoforming. Doctoral dissertation, Université du Québec en Abitibi-Témiscamingue, Quebec, Canada.

[29] Basiji, F., Erchiqui, F., Koubaa, A., & Ghasemi, I. (2025). Influence of fiber concentration and length on the dielectric, mechanical, and thermal properties of maple wood fiber-reinforced polypropylene. Journal of Thermoplastic Composite Materials. doi:10.1177/08927057251319772.

[30] Lodge, A. S. (1964). Elastic liquids. Academic Press, New York, United States.

[31] Bernstein, B., Kearsley, E. A., & Zapas, L. J. (1963). A study of stress relaxation with finite strain. Transactions of the Society of Rheology, 7(1), 391-410. doi:10.1122/1.548963.

[32] Lodge, A. S. (1964). Elastic liquids: An introductory vector treatment of finite-strain polymer rheology. Academic Press, New York, United States.

[33] Reddy, J. N. (1993). An introduction to the finite element method. McGraw-Hill, New York, United States.

[34] Koffi, A., Mijiyawa, F., Koffi, D., Erchiqui, F., & Toubal, L. (2021). Mechanical properties, wettability and thermal degradation of HDPE/birch fiber composite. Polymers, 13(9), 1459. doi:10.3390/polym13091459.

[35] Adhikari, R., & Wood, D. (2018). The design of high efficiency crossflow hydro turbines: A review and extension. Energies, 11(2), 267. doi:10.3390/en11020267.

[36] Quaranta, E., Perrier, J. P., & Revelli, R. (2022). Optimal design process of crossflow Banki turbines: Literature review and novel expeditious equations. Ocean Engineering, 257, 111582. doi:10.1016/j.oceaneng.2022.111582.

[37] Mockmore, C. A. (1949). The Banki water turbine. Engineering Experiment Station, Oregon State College, Oregon, United States.

[38] Leguizamón, S., & Avellan, F. (2020). Computational parametric analysis of the design of cross-flow turbines under constraints. Renewable Energy, 159, 300-311. doi:10.1016/j.renene.2020.03.187.

[39] Kifumbi, F., Ngoma, G. D., Kabeya, P., & Umba-di-Mbudi, C. N. Z. (2022). Design and Modeling of a Numerical Simulator of a Mini-hydropower for Performance Characterization of the Turbine Type of Francis, Cross-flow and Pelton. SIMULTECH, 1, 226-233. doi:10.5220/0011265000003274.

[40] Adanta, D., Sari, D. P., Syofii, I., Thamrin, I., Yani, I., Marwani, Fudholi, A., & Prakoso, A. P. (2024). Configuration blade shape for enhancement crossflow turbine performance by the CFD method. International Journal of Thermofluids, 22, 100665. doi:10.1016/j.ijft.2024.100665.

[41] Galvis-Holguin, S., Rio, J. S. Del, González-Arango, D. I., Correa-Quintana, E., & Meneses, L. D. R. (2025). Numerical and Experimental Validation of a New Methodology for the Design of Michel-Banki Turbine. CFD Letters, 17(5), 76–89. doi:10.37934/cfdl.17.5.7689.

[42] Kumar, G., & Nair, A. G. (2025). Dominant balance-based adaptive mesh refinement for incompressible fluid flows. Journal of Computational Physics, 114522. doi:10.1016/j.jcp.2025.114522.

[43] López-Pachón, M., & Marcé-Nogué, J. (2025). The crucial role of meshing in computational fluid dynamics simulations for organic geometries in paleobiology: Describing fluid dynamics performance through best practices. Methods in Ecology and Evolution, 16(10), 2170–2194. doi:10.1111/2041-210X.70146.

[44] Abbas, A., Alam, M., & Kumar, R. (2020). Analytical analysis of combined effect of interior guide tube and draft tube on cross flow turbine performance. Materials Today: Proceedings, 46, 5372–5377. doi:10.1016/j.matpr.2020.08.796.

[45] Tesfay, A. H., Weldemariam, S. A., & Gebrelibanos, K. G. (2025). Design and Development of Crossflow Turbine for Off-Grid Electrification. Energies, 18(19), 5108. doi:10.3390/en18195108.